

# Kinematics and Metallicity of M31 Red Giants: The Giant Southern Stream and Discovery of a Second Cold Component at $R = 20$ kpc

Jasonjot S. Kalirai<sup>3,4</sup>, Puragra Guhathakurta<sup>3</sup>, Karoline M. Gilbert<sup>3</sup>, David B. Reitzel<sup>5</sup>,  
Steven R. Majewski<sup>6</sup>, R. Michael Rich<sup>5</sup>, and Michael C. Cooper<sup>7</sup>

## ABSTRACT

We present spectroscopic observations of red giant branch (RGB) stars in the Andromeda spiral galaxy (M31), acquired with the DEIMOS instrument on the Keck II 10-m telescope. The three fields targeted in this study are in the M31 spheroid, outer disk, and giant southern stream. In this paper, we focus on the kinematics and chemical composition of RGB stars in the stream field located at a projected distance of  $R = 20$  kpc from M31's center. A mix of stellar populations is found in this field. M31 RGB stars are isolated from Milky Way dwarf star contaminants using a variety of spectral and photometric diagnostics. The radial velocity distribution of RGB stars displays a clear bimodality — a primary peak centered at  $\bar{v}_1 = -513$  km s<sup>-1</sup> and a secondary one at  $\bar{v}_2 = -417$  km s<sup>-1</sup> — along with an underlying broad component that is presumably representative of the smooth spheroid of M31. Both peaks are found to be dynamically cold with intrinsic velocity dispersions of  $\sigma(v) \approx 16$  km s<sup>-1</sup>. The mean metallicity and metallicity dispersion of stars in the two peaks is also found to be similar:  $\langle [\text{Fe}/\text{H}] \rangle \sim -0.45$  and  $\sigma([\text{Fe}/\text{H}]) = 0.2$ . The observed velocity of the primary peak is consistent with that predicted by dynamical models for the stream, but there is no obvious explanation for the secondary peak. The nature of the secondary cold population is unclear: it may represent: (1) tidal debris from a satellite merger event that is superimposed on, but unrelated to, the giant southern stream; (2) a wrapped around component of the giant southern stream; (3) a warp or overdensity in M31's disk at  $R_{\text{disk}} > 50$  kpc (this component is well above the outward extrapolation of the smooth exponential disk brightness profile).

*Subject headings:* galaxies: individual (M31) – galaxies: structure – techniques: spectroscopic

---

<sup>1</sup>Data presented herein were obtained at the W. M. Keck Observatory, which is operated as a scientific partnership among the California Institute of Technology, the University of California, and the National Aeronautics and Space Administration. The Observatory was made possible by the generous financial support of the W. M. Keck Foundation.

<sup>2</sup>Based on observations obtained with MegaPrime/MegaCam, a joint project of CFHT and CEA/DAPNIA, at the Canada-France-Hawaii Telescope (CFHT) which is operated by the National Research Council (NRC) of Canada, the Institut National des Science de l'Univers of the Centre National de la Recherche Scientifique (CNRS) of France, and the University of Hawaii.

<sup>3</sup>University of California Observatories/Lick Observatory, University of California at Santa Cruz, 1156 High Street, Santa Cruz, California 95064, USA; jkalirai@ucolick.org

<sup>4</sup>Hubble Fellow

<sup>5</sup>Department of Astronomy, University of California at Los Angeles, Box 951547, Knudsen Hall, Los Angeles, California 90095, USA

<sup>6</sup>Department of Astronomy, University of Virginia, P. O. Box 3818, Charlottesville, Virginia 22903, USA

<sup>7</sup>Astronomy Department, 601 Campbell Hall, University of California at Berkeley, Berkeley, California 94720, USA

## 1. Introduction

Non-baryonic matter is now known to comprise a significant fraction (23%) of the total matter/energy content of the Universe (Spergel et al. 2003). It is generally believed that this matter is most likely in the form of weakly interacting cold dark matter (CDM). Cosmological simulations suggest that the large-scale distribution of matter in the Universe is consistent with CDM predictions (i.e., observations of galaxy clustering). Simulations also suggest that the evolution of this dark matter imprints a signature on much smaller scales. In fact, it is expected that CDM will cluster gravitationally on subgalactic scales. Within the framework of hierarchical formation scenarios (Searle & Zinn 1978), it is the merging and accretion of these subhalos that is thought to build up massive galaxies such as the Milky Way and our neighbor the Andromeda spiral galaxy (M31).

The cores of the CDM subhalos that fall into massive potentials to form large galaxies are expected to remain intact, even after experiencing strong tides through several orbital timescales around the host galaxy (Hayashi et al. 2003). A fraction of the subhalos will have also likely experienced star formation either prior to, or during assimilation with the host. A parent galaxy the size of the Milky Way or M31 may be expected to have cannibalised, or at the least be host to, 100–500 dwarf galaxy mass systems over its lifetime (e.g., Klypin et al. 1999; Moore et al. 1999; Bode, Ostriker, & Turok 2001).

Numerical simulations suggest that the accretion of dwarf galaxies by massive hosts should leave fossil signatures in the form of tidal streams around massive galaxies (Johnston 1998; Bullock, Kravtsov, & Weinberg 2001). The Sagittarius dwarf galaxy (Ibata, Gilmore, & Irwin 1994; Majewski et al. 2003) is an excellent example of such a merger in our own Galaxy. Other merger events are also seen in the Milky Way, such as the Magellanic stream (Mathewson, Cleary, & Murray 1974) and the Monoceros stream (Yanny et al. 2003). The recent discovery of the giant stellar stream to the south of M31 (Ibata et al. 2001) confirms that tidal streams are in fact a remnant of the accretion process, and that this process is still occurring today in galaxies. Studying the dynamics, composition, and structure of these streams will help produce a clear picture of the recent accretion history of these host galaxies and further help constrain what fraction of halos may originate in these accretion events. In some ways such studies are more easily carried out in M31 than the Milky Way since our location within the latter cause local streams to have a larger angular extent and lower stellar density on the sky. The giant stellar stream of M31 is of particular interest as it is easily seen in optical star-count maps spanning over a very large radial extent ( $>125$  kpc), and therefore can set important constraints on the potential of M31 (e.g., Geehan et al. 2005).

## 2. Previous Studies of the M31 Giant Southern Stream

Since its discovery by Ibata et al. (2001), the giant southern stream in M31 has been the focus of many scientific papers. The brightest red giant branch (RGB) stars in the stream have  $I_0 \approx 20.5$ , and therefore have been targeted with both imagers and spectrographs in ground- and space-based studies. The spatial extent of the stream has now been mapped in the south-east direction from an outermost field at a projected radial distance of  $\sim 60$  kpc to an inner field at  $\sim 10$  kpc from the center of M31 (Ferguson et al. 2002; Ibata et al. 2004). Based on fits to the tip of the RGB, the line of sight distances to stars in the outer regions of the stream indicate that these regions are located  $\sim 100$  kpc behind M31 (McConnachie et al. 2003). On the north-west side, the stream can be traced to a point where it is  $\sim 40$  kpc in front of M31 (McConnachie et al. 2003).

Spectroscopic studies along the path of the stream have provided both abundance and kinematical

measurements for its constituent stars as a function of radial distance from M31’s center. Ibata et al. (2004) obtained Keck/DEIMOS spectra in four fields spanning a range of radial distances in the southern quadrant of M31. Their data show that at the outer regions of the stream, stars are moving with a heliocentric velocity of  $v = -320 \text{ km s}^{-1}$  (i.e., at approximately the systemic velocity of M31). However, closer to M31 (in Ibata et al.’s field 6 at a projected radius of  $R \sim 25 \text{ kpc}$ ), the stream stars are blueshifted by an additional  $160 \text{ km s}^{-1}$ . In their innermost field ( $R \sim 12 \text{ kpc}$ ), Ibata et al. only find 2–4 likely stream stars moving with a heliocentric velocity of  $v_{\text{hel}} = -520 \text{ km s}^{-1}$ . Over its radial extent, the velocity distribution of stream stars shows a very sharp negative edge based on these studies. The velocity dispersion is found to be very narrow,  $\sigma_v = 11 \pm 3 \text{ km s}^{-1}$ . Guhathakurta et al. (2005a) provide further Keck/DEIMOS observations of 45 bona-fide stream members located in a field at a projected distance of  $\sim 33 \text{ kpc}$  from the center of M31 (between two of the Ibata et al. 2004 pointings). By deconvolving the general halo population from the stream, they find that the stream is both more metal rich ( $\langle [\text{Fe}/\text{H}] \rangle = -0.51$ ) and contains a much smaller metallicity dispersion (0.25 dex) than the general halo. At this location, the heliocentric velocity of the stream is found to be  $v = -458 \text{ km s}^{-1}$  with a low internal line-of-sight velocity dispersion ( $\sigma_v = 15^{+8}_{-15} \text{ km s}^{-1}$ ).

The Andromeda giant stream has now been studied with imaging/spectroscopy over a 125 kpc radial extent. This work has shed light on the dynamics, orbit, and metallicity of the stream, and put constraints on the progenitor galaxy (Fardal et al. 2005). From analyzing the width and velocity dispersion of the debris, Font et al. (2005) find that the progenitor of the stream must have been a dwarf galaxy with a mass of at least  $10^8 M_{\odot}$ . The orbit of this progenitor is believed to have been highly eccentric and close to edge on, passing very close to the nucleus of M31 (within 2 kpc of M31’s center — Ibata et al. 2004; Font et al. 2005; Fardal et al. 2005). The high surface brightness of the stream indicates that this passage occurred within the past few Gyr at most (Ibata et al. 2004; Fardal et al. 2005).

Despite the wealth of knowledge that we have on the Andromeda stream, many important questions remain unanswered. If it still exists, the progenitor galaxy has yet to be identified although there are several interesting candidates. These include the claimed tidally distorted satellite galaxy And VIII (Morrison et al. 2003) or the concentration found in the distribution of M31 planetary nebulae (Merrett et al. 2003). Also unclear is whether the stream does in fact extend to the north-west side of M31, in front of the galaxy, as suggested by McConnachie et al. (2003). No spectroscopic observations have yet been obtained in this region of M31. Finally, given their very small pericenter, stream stars have almost certainly been, and will continue to be, stripped from their progenitor and subsequently injected into the general halo of M31 (Ibata et al. 2004). This “pollution” potentially makes it very difficult to interpret age/metallicity measurements in the “smooth” halo and needs to be characterized. For example, the recent discovery of an intermediate age population of stars in the spheroid of M31 (Brown et al. 2003) may represent stream contamination (Ferguson et al. 2005).

To answer some of these important questions, we have begun a large program to obtain Keck/DEIMOS spectroscopy of M31 RGB stars. The three spectroscopic fields presented in this paper were chosen to directly overlap recent ultra-deep *Hubble Space Telescope* (*HST*)/Advanced Camera for Surveys imaging pointings of M31 (P.I. T. Brown - Cycle 13): (1) a spheroid field on the south-east minor axis located at  $R = 12.2 \text{ kpc}$  (H11), (2) a stream field located at  $R = 21.3 \text{ kpc}$  (H13s), and (3) a disk field on the north-east major axis at  $R = 25.8 \text{ kpc}$  (H13d). The distances given here apply to our spectroscopic field centers and not the *HST*/ACS field centers. In this contribution, we present the observations and data reduction for all three fields (§ 3), as well as a brief discussion on obtaining a clean sample of bonafide M31 RGB stars in each field (§ 4). The imaging observations are analyzed in § 5, where we present both color-magnitude diagrams (CMDs) and derive photometric metallicities for our sample. The spectroscopic observations are presented in

§ 6. This includes determining the chemical composition and kinematics of stars in each field, with particular focus on the stream observations. These data are analyzed and discussed in § 7. Ongoing and future projects are highlighted in § 8 and the conclusions of the present study are given in § 9. Forthcoming papers will present additional analysis of the data in fields H11 and H13d.

### 3. Observations and Data Reduction

The locations of the stream (H13s), spheroid (H11), and disk (H13d) spectroscopic fields presented in this study are shown as white rectangles superimposed on a star-count map of M31 (Ferguson et al. 2002; Ibata et al. 2005) in Figure 1. For H13s and H11, two spectroscopic observations were obtained at the same right ascension ( $\alpha$ ) and declination ( $\delta$ ), but with different mask position angles. For H13d, the same position angle was used for both masks. The giant southern stream can be clearly seen extending radially outward in the south-east region. Fields studied in other papers as discussed earlier are shown as open circles (see § 7.2.2).

#### 3.1. Imaging Fields and Astrometry

RGB candidates were selected as targets for the Keck/DEIMOS spectrograph from CFHT/MegaCam photometry for the H13s and H11 fields, and from Keck/DEIMOS imaging for the H13d field. The MegaCam pointings, each covering 1 degree<sup>2</sup>, are at relatively small radial distances from M31: one is directly along the south-east minor axis and the other is centered on the giant southern stream. The MegaCam images overlap with the much smaller Keck/DEIMOS fields ( $16' \times 4'$ ). For the wide-field photometry, we obtained three 1160s exposures with MegaCam in each of the  $g'$  and  $i'$  filters, for both pointings. All MegaCam images were obtained in photometric conditions, with sub-arcsecond seeing (most images have  $0''.6$ – $0''.8$ ) and airmasses less than 1.3. The  $g'$  and  $i'$  photometry from CFHT/MegaCam was converted in Johnson-Cousins  $V$  and  $I$  using standard star fields.

Astrometric solutions were built from the CFHT images using several steps (P. Stetson 2004, private communication). First, the US Naval Observatory USNO-A2.0 Guide Star Catalog (Monet et al. 1998) was used to extract all standards falling within either of the MegaCam pointings. Stellar positions were then measured on overlapping Digitized Sky Survey plates using a modernized version of the Stetson (1979) software. Coordinates in these files, and those from an ALLFRAME analysis of the CFHT/MegaCam images, were all put onto a common reference frame using ten-parameter cubic fits in  $x$  and  $y$  within DAOMASTER. The resulting files contain  $x$  and  $y$  in arcseconds, increasing to the east and north, respectively, based on a primary reference frame of the USNO-A2.0 positions. The accuracy of the coordinates from this transformation, based on fitting the residuals, is better than  $0''.1$  (see § 2.2 of Stetson, McClure, & VandenBerg 2004 for more information).

Relevant sections of the 1 degree<sup>2</sup> CFHT image that overlapped the Keck/DEIMOS masks were extracted from each of the three 1160s exposures, for each filter. These were bias subtracted, flat fielded, shifted and combined using the FITS Large Images Processing Software (FLIPS) developed at CFHT (J.-C. Cuillandre, 2001, private communication). More information on FLIPS can be found in § 3.1 of Kalirai et al. (2001). For the processed  $g'$  and  $i'$  images, we used SExtractor (Bertin & Arnouts 1996) to produce a

catalog of all stars, and applied the above transformation to derive  $\alpha$  and  $\delta$  (J2000) using the standard IRAF<sup>1</sup> tasks CCMAP and CCTRAN.

For H13d, 1–300s imaging exposure was obtained using Keck/DEIMOS in July 2004 by replacing the grating with a mirror. This field was also obtained at low airmass (1.11) and good seeing ( $0''.7$ ). An astrometric solution was built for each of the 4 CCDs based on manually aligning 10–15 USNO standard stars per CCD with their observed centers. The derived transformation was applied to the remaining stars, giving  $\alpha$  and  $\delta$  (J2000).

### 3.2. Multi-object Spectroscopic Masks

Target selection and slitmask design for Keck/DEIMOS spectroscopy were carried out using a very similar method to that described in Guhathakurta et al. (2005a). Summarizing, we first assign a priority to each object based primarily on its magnitude ( $20.5 < I_0 < 22.5$ ) and stellarity (morphology index from SExtractor used to distinguish stars from galaxies). These priorities are fed into the **dsimulator**<sup>2</sup> software program, which builds the most efficient mask by maximizing the number of top priority objects first, and then subsequently adding lower priority stars. These lower priority stars are primarily those with fainter magnitudes, and will therefore have a lower signal-to-noise (S/N) spectra. The program prevents any overlapping slits and ensures both a small gap  $0''.5$  in the spatial direction between any two slits and a minimum length of  $6''$  for each slitlet. Predicted locations of the inter-CCD gaps and vignetted regions are avoided. All slits were produced with a width of  $1''$ . This procedure allowed for  $\sim 150$  slits to be cut on each mask. We note that we have yet to recover spectra for  $\sim 12.5\%$  of the slits in our H13s and H11 fields due to problems with slit extraction. The missing slits are all located on two of the DEIMOS eight CCDs and it is yet unclear why the extractions for these objects failed.

Two spectroscopic masks were constructed for each of H13s, H11, and H13d. For H13s and H11, we offset the position angle by  $\pm 21.0$  degrees for the two pointings. The central  $\alpha$  and  $\delta$  are identical, thereby allowing for a small overlap in the database of available stars for each mask. Two stars in each of these fields were observed twice. For H13d, a position angle of  $+27.8$  was used for both masks to allow two spectra to be obtained for 53 objects.

### 3.3. Spectroscopic Observations

The six multislit masks (two for each of the H11, H13s, and H13d fields) were observed using the Keck II 10-m telescope and DEIMOS spectrograph on 2004 September 20 (UT). We obtained  $3 \times 20$  min exposures for each mask at relatively low airmass ( $< 1.3$ ). The grating used for the spectroscopy has 1200 lines  $\text{mm}^{-1}$  and a dispersion of  $0.33\text{\AA} \text{ pixel}^{-1}$ . The grating tilt was chosen such that the central wavelength was about  $7800\text{\AA}$ , thereby providing spectral coverage in the range  $\approx 6400\text{--}9100\text{\AA}$ . The resolution of the spectra is  $1.3\text{\AA}$  (FWHM) for typical  $0''.8$  FWHM seeing.

The targeted fields are shown in Figure 1 superimposed on a star-count map of M31. For the stream

---

<sup>1</sup>IRAF is distributed by the National Optical Astronomy Observatories, which are operated by the Association of Universities for Research in Astronomy, Inc., under cooperative agreement with the National Science Foundation.

<sup>2</sup>[http://www.ucolick.org/~phillips/deimos\\_ref/masks.html](http://www.ucolick.org/~phillips/deimos_ref/masks.html)

field, H13s, we observe the two pointings at a radial distance of 21.3 kpc from the center of M31. For the spheroid field, H11, we observe both pointings on the south-east minor axis located at  $R = 12.2$  kpc. For the disk field, H13d, we observe both pointings on the north-east major axis at  $R = 25.8$  kpc.

Table 1 summarizes the spectroscopic observations, positions of the fields, and numbers of targets observed on each mask.

### 3.4. Spectroscopic Data Reduction

The six DEIMOS masks were processed using the **spec2d**<sup>3</sup> software pipeline (v1.1.4) developed by the DEEP2 team at the University of California-Berkeley (UCB). A summary of the steps involved in the data reduction including the flat-fielding, fringe correction, wavelength calibration, sky subtraction, cosmic-ray rejection, and extraction can be found in Guhathakurta et al. (2005a).

### 3.5. Velocity Measurements and Quality Assessment

The final extracted spectra are next processed through the **spec1d**<sup>4</sup> software pipeline, also developed by the DEEP2 team at UCB. This software cross-correlates the observed spectrum with a large database of both template stellar spectra (multiple A, B, F, G, K, L, M type, and Carbon star) and template emission- and absorption-line galaxy spectra to determine the red/blueshift for all objects. The results are displayed in the visual inspection software **zspec** (developed by D. Madgwick for the DEEP2 survey). In rare cases, the automated cross-correlation failed despite the presence of obvious spectral features upon visual inspection (e.g., due to artifacts from poorly subtracted night sky lines). For these cases (7% of all targets with such features), the radial velocity was manually determined using any of several spectral features: the Ca II triplet, the Na I doublet (dwarfs), and/or the 7100Å TiO band. The typical signal-to-noise of these spectra is  $\sim 10$  per pixel. The velocity uncertainty from the cross-correlation is empirically estimated to be  $\sim 10$  km s<sup>-1</sup> from the 57 objects that were observed twice (see § 2.4 of Gilbert et al. 2005, in preparation) in H13s, H11, and H13d.

A heliocentric velocity correction was applied to each of the fields using the IRAF task RVCOR. The corrections were determined to be +12.17 km s<sup>-1</sup> for H13s, +12.45 km s<sup>-1</sup> for H11, and +13.0 km s<sup>-1</sup> for H13d.

In addition to the radial velocity measurements, which are based on the cross-correlation of all features in the spectrum, we also assign a spectral quality index to each object based on what spectral features are obvious/visible relative to the noise. Spectra with two or more definite absorption/emission lines were assigned a spectral quality index of  $Q = 4$ , while spectra with one definite and one marginal line were assigned  $Q = 3$ . Spectra for which a radial velocity could not be determined due to poor S/N and/or spectra that showed a lack of definite features were assigned  $Q = 2$  (255 objects). Spectra with extremely poor S/N were assigned  $Q = 1$ , and spectra affected by instrumental artifacts (bad columns, CCD edges, vignetting, etc.) were assigned  $Q = -2$ . Of the 830 spectra obtained on these 6 masks, only 2 objects were assigned  $Q = -2$  and 4 objects were assigned  $Q = 1$ . These objects will be ignored from here on.

---

<sup>3</sup><http://astron.berkeley.edu/~cooper/deep/spec2d/primer.html>

<sup>4</sup><http://astron.berkeley.edu/~cooper/deep/spec1d/primer.html>

Figure 2 presents the distribution of  $I_0$  magnitudes for objects on the two H13s masks with spectral quality index  $Q = 2, 3$ , and 4. The distribution of  $Q = 4$  objects is clearly shifted towards brighter apparent magnitudes than the rest. The  $Q = 2$  category comprises most of the faint spectroscopic targets. The bulk of the  $Q = 3$  objects lie between the other two categories. This figure clearly indicates that our spectral quality indices are correlated with the S/N in our data (i.e., a large number of stars have been classified as  $Q = 2$  precisely because they are fainter and have lower S/N than the rest of the sample).

In Figure 3 (left) we present spectra of 30 M31 RGB stars in the H13s stream field, displaying an 800Å portion in the region of the Ca II triplet: 8498, 8542, and 8662Å (the full spectra cover a 2700Å range, centered on  $\approx 7800$ Å). The stars whose spectra are shown in this plot span the entire brightness range over which we have assigned a spectral quality index of  $Q = 4$  (see Fig. 2). In Figure 3 (right) we zoom into the Ca II triplet region for three arbitrarily chosen stars with  $I_0 = 20.87, 21.46$ , and  $21.96$ . At this scale, it is clear that the spectra also show several other absorption features within this narrow wavelength window, such as Fe I lines at  $\sim 8517$ Å and  $\sim 8690$ Å (see middle and bottom right panels).

#### 4. Removing Contaminants

The line of sight to M31 encounters both foreground and background contamination. Although extragalactic objects can be removed from image morphology and radial velocity alone, a clear study of M31’s stellar populations also requires the removal of Milky Way disk/halo stars. In radial velocity space, these dwarfs often overlap M31 giants and can therefore be indistinguishable. For example, our H13d pointing encounters M31’s disk in the north-east quadrant, where the disk is redshifted relative to M31’s  $\sim -300$  km s $^{-1}$  blueshift. Therefore, these stars will have low radial velocities, similar to those for Galactic dwarfs.

We have developed a sensitive technique to eliminate Milky Way contaminants from our study of M31 stars. The method uses probability distribution functions calculated from a training set of known RGB and dwarf stars. Using four criteria: (1) radial velocity, (2) Na I equivalent width (surface gravity sensitive), (3) position in the CMD, and (4) comparison between photometric and spectroscopic [Fe/H] measurements, each star is assigned four likelihood values of being a giant or a dwarf based on its value within each diagnostic. The details of this procedure are given in Gilbert et al. (2005, in preparation), along with one other diagnostic that was not available for these fields (*DDO51* parameter). Here we provide a few details and present the separation of RGB from dwarf stars in just the stream field, H13s.

In Figure 4, the probability distribution functions for each of the four diagnostics discussed above are given. The darker solid curves denote the RGB training set population whereas the dashed or thinner curves represent the dwarf training set. Clearly, the probability distribution functions have different shapes although there is some overlap. The probability of any given star in our study being a RGB and a dwarf is calculated given its properties within each of these diagnostics and the corresponding probability distribution functions. In this Figure, we also overplot the H13s stars within each diagnostic. For  $v_{\text{hel}}$ , the H13s stars are shown as histograms for calculated RGB stars (solid) and dwarfs (dashed). The H13s RGB histogram is offset from the training set RGB curve given the large negative velocities of stream stars in this field (our training set is drawn from mostly RGB stars in M31’s spheroid). For the other three diagnostics, the RGB stars are shown as larger open circles and the dwarfs are shown as smaller crosses. In all panels, the confirmed RGB and dwarf stars follow the appropriate probability distribution function.

As discussed in Gilbert et al. (2005, in preparation), the individual probabilities from each of these four diagnostics are combined to yield the final discriminant of whether the star is a bona-fide M31 giant. This

overall likelihood ( $\Sigma L_i$ ), for H13s stars, is presented in Figure 5. The results show a very nice bi-modal distribution with RGB stars ( $\Sigma L_i > 0$ ) and dwarf stars ( $\Sigma L_i < 0$ ) well separated. Therefore, although none of the individual diagnostics used to measure the probability distribution functions provide a perfect discriminant of RGB stars and dwarfs (with the exception of radial velocity, in the rare case of stream stars), the combination of the four diagnostics provides a powerful tool.

The remainder of our analysis focuses on a sample of M31 RGB stars cleaned by the above process.

## 5. Imaging/Photometric Analysis

### 5.1. Color-Magnitude Diagrams

In Figure 6, we present CMDs for each of the H13s (top) and H11 (bottom) fields. The objects for which we obtained a spectra are shown as larger symbols in either panel. These were selected to be bright enough for good S/N in one hour exposures with Keck, and therefore have  $20.5 \lesssim I_0 \lesssim 22.5$ . The remaining objects (shown as smaller dots) represent the CFHT photometry for a very small section of the MegaCam image, equal to approximately 1 out of the 36 chips on the mosaic ( $\approx 96 \text{ arcmin}^2$ ), centered at the DEIMOS pointing. In the CFHT photometry for H13s, there are a total of  $\sim 2400$  stars with  $20 \lesssim I_0 \lesssim 22.5$ . Scaling this to the size of the DEIMOS footprint gives  $\sim 2600$  objects. This is calculated using the area of two masks ( $16' \times 4'$  each), and subtracting the area of the overlap region ( $23.9 \text{ arcmin}^2$ ). Of these, 270 (10%) were targeted for spectroscopy in our two masks.

Reddening corrections have been applied to the data using the Schlegel, Finkbeiner, & Davis (1998) reddening maps. For H13s, the correction is found to be  $E(V - I) = 0.08$  and for H11 it is  $E(V - I) = 0.10$ . Each of the CMDs clearly shows the RGB of M31 extending from the faintest stars ( $I_0 \sim 25$ ) up to the tip of the RGB at  $I_0 \sim 20.5$ . For clarity, we have also overplotted several theoretical isochrones from Girardi et al. (2002) ranging in metallicity from  $Z = 0.0001$  or  $[\text{Fe}/\text{H}] = -2.3$  (bluest isochrone) to  $Z = 0.03$  or  $[\text{Fe}/\text{H}] = +0.2$  (reddest isochrone) for  $t = 12.6 \text{ Gyr}$ . A distance modulus of  $(m - M)_0 = 24.47$ , corresponding to a distance of 783 kpc, has been applied to the isochrones.

The left panels of Figure 6 show the cleaned sample of confirmed M31 RGB stars in the stream and spheroid (i.e., those that have passed a  $Q = 3$  or 4 cut, and survived the dwarf star contamination rejection routines discussed in § 4). The panels on the right show confirmed Milky Way dwarfs (open circles),  $Q = 2$  objects (filled squares), and galaxies (crosses) within each of these fields. As expected, most of the Milky Way dwarfs are located above the tip of the RGB and most of our  $Q = 2$  objects represent the faintest stars for which we obtained a spectrum. The cleaned sample of stream stars (top-left) also shows a few confirmed M31 giants that are above the tip of the RGB. These are potentially intermediate aged asymptotic giant branch (AGB) stars. Only minor differences exist between the metallicity distributions of stars in these fields. As discussed in § 3.2, the selection process involved picking stars within a magnitude range and did not bias the color selection. The majority of the stars in the spheroid field appear to have a similar metallicity and metallicity dispersion, than the stream.

### 5.2. Photometric Metallicities

In order to compute photometric metallicities for these stars, we used a very large grid of finely spaced ( $\Delta Z = 0.0001$ ) isochrones of age 12.6 Gyrs and  $[\alpha/\text{Fe}] = 0$  (L. Girardi 2004, private communication). The



metallicity of each star was derived using a nearest neighbor method within this grid. The most metal-poor isochrone used was  $Z = 0.0001$  ( $[\text{Fe}/\text{H}] = -2.3$ ) while the most metal-rich isochrone had  $Z = 0.03$  ( $[\text{Fe}/\text{H}] = +0.2$ ), resulting in over 300 isochrones and 15,000 data points within the region of interest in the CMD. We used linear extrapolation to “pad” the isochrones to accommodate stars that lie beyond the bounds of the models in the CMD. For the brighter data points, the standard isochrones were extrapolated brightward and for the bluer/redder data points, we produced “cross-isochrones” by connecting the models with different  $Z$ , yet the same mass, and extrapolated those (see Fig. 7). These “cross-isochrones” were also used in the separation of Milky Way dwarfs from M31 giants as discussed in § 3.5 of Gilbert et al. (2005, in preparation). As can be seen from Figure 7, this extrapolation was needed for very few stars thus minimizing any possible contamination from treating an AGB star as a RGB star.

In Figure 8 (top), we present the photometric metallicity distributions for stars in H13s (solid line). For the best fit Gaussian (dashed curve), we find  $\langle [\text{Fe}/\text{H}] \rangle = -0.45$ ,  $\sigma([\text{Fe}/\text{H}]) = 0.24$ . Also shown is a Gaussian representing the metallicity distribution of stars in our spheroid field, H11 (dotted curve - Rich et al. 2005, in preparation). The mean metallicity of the stream field is clearly similar to that of the spheroid, and with a similar dispersion. Guhathakurta et al. (2005a) find the stream’s metallicity to be similar ( $[\text{Fe}/\text{H}] = -0.54$ ) at a location 31 kpc from the center of M31 (i.e., 10 kpc further out). The metallicity dispersion in their work ( $\sigma([\text{Fe}/\text{H}]) = 0.25$ ) is also very similar to that found in this study,  $\sigma([\text{Fe}/\text{H}]) = 0.24$ . As a cautionary note, we point out that the relative measurement of photometric metallicity within a given population is more accurate than the absolute comparison of different populations. The latter will be more affected by several uncertainties: possible age spreads between the populations,  $[\alpha/\text{Fe}]$  variations, differential reddening, etc. The middle and bottom panels of Figure 8 will be discussed in § 7.2.1.

## 6. Spectroscopic Analysis

### 6.1. Spectroscopic Metallicities

We derive spectroscopic metallicities for RGB stars in this work based on the line strength of the Ca II triplet ( $\lambda \sim 8500\text{\AA}$ ). These are computed on the Carretta & Gratton (1997) scale. This procedure is described in detail in Reitzel & Guhathakurta (2002) and Guhathakurta et al. (2005a). Summarizing, the equivalent widths of the three individual Ca II lines are measured and combined to yield a reduced equivalent width according to Rutledge, Hesser, & Stetson (1997). An empirical calibration based on Galactic globular cluster RGB stars was used to calculate  $[\text{Fe}/\text{H}]_{\text{spec}}$  from the equivalent widths (Rutledge et al. 1997). A value of  $V_{\text{HB}} = 25.17$  (Holland 1996) was adopted for the luminosity-based correction of surface gravity. This comes from *HST* observations of M31 HB in nearby fields. This measurement, from equivalent widths, is known to have a relatively large uncertainty in it compared to the random error in  $[\text{Fe}/\text{H}]_{\text{phot}}$ , yielding an inflated spread in metallicities. The two however are consistent on a global scale, as shown in § 5.2 of Guhathakurta et al. (2005a).

### 6.2. Kinematics

As discussed in § 3.5, we measure velocities for all stars by cross-correlating the observed spectrum with template spectra over a range of velocities. In Figure 9 we present velocity histograms for M31 stars in H13s, H11, and H13d. The histograms show a clear separation of M31’s stellar populations, based solely on kinematics. As expected, the stream field at  $R \sim 21$  kpc shows a large number of highly blueshifted stars as

well as some evidence of a weakly detected smooth spheroid. We also see a distinct, cold secondary peak of M31 stars at a slightly less negative velocity. Such a bimodal velocity distribution has never been reported before and may contain important information related to the orbit of the giant southern stream, or the discovery of a new stream (see discussion below). The H11 minor-axis field shows a much hotter population of stars (presumably spheroid) centered near M31’s systemic velocity. The H13d major-axis field in the north-east quadrant shows a dominant cold population superimposed on a smooth spheroid. The velocity of this cold component is generally consistent with M31’s disk rotation in this field (i.e., the disk is rotating away from the line of sight in this quadrant causing a relative redshift of stars on top of the  $\sim -300$  km s $^{-1}$  systemic blueshift).

We focus now on the kinematics of the H13s population shown in Figure 9 (top). The velocity histogram is well fit by the sum of three Gaussians (dotted line): the two prominent cold peaks in velocity space, and the broad underlying smooth component. For the best fit, we find the mean velocity of stars in the primary peak is  $\bar{v}_1 = -513$  km s $^{-1}$  and  $\sigma(v_1) = 19$  km s $^{-1}$ . For the secondary peak, we find  $\bar{v}_2 = -417$  km s $^{-1}$  and  $\sigma(v_2) = 19$  km s $^{-1}$ . The Gaussian representing the smooth spheroid of M31 is held fixed at  $\bar{v}_3 = -310$  km s $^{-1}$  ( $\sigma(v_3) = 85$  km s $^{-1}$ ), as constrained from our H11 field.

The dispersion quoted above includes the intrinsic dispersion of the population and our measurement error. We estimate the latter by comparing the velocity measurements of stars that were observed twice, largely in the H13d field. The brightnesses and S/N of those spectra are virtually identical to the H13s stars, and therefore the measurement errors will be similar for both. For the mean S/N acquired (8.8 in H13s), we find that the velocity measurement error is 10.89 km s $^{-1}$ . Subtracting this in quadrature from the measured  $\sigma(v_1)$  and  $\sigma(v_2)$  above, we find that the velocity dispersions of stars is 16 km s $^{-1}$  in the primary and secondary peaks.

Of the 104 stars in the H13s radial velocity histogram, the triple Gaussian fit to the cumulative distribution suggests that 50.5% of the stars are in the primary narrow peak corresponding to the giant southern stream (53 stars), 26.5% are in a second narrow peak (28 stars), and 23% are in the broad spheroidal component (24 stars). The contamination of spheroid stars into either of our primary or secondary peaks is negligible. Guhathakurta et al. (2005b) compute a surface brightness from the spheroid component in H13s and find that these data agree well with the known M31 surface brightness profile. In the next section, we consider the properties of the primary and secondary cold peaks. We note that the CMD positions of stars in both peaks in the CMD are indistinguishable.

## 7. Discussion

### 7.1. Giant Southern Stream

As described in §2 the velocity gradient of the giant stream has now been mapped in several small pointings over a 125 kpc radial extent (Figure 1 shows the approximate locations of these pointings). With respect to these pointings, our H13s field is located very close to the center of M31 ( $R \sim 21$  kpc). Within this radius, only one study has kinematically confirmed stream members (Ibata et al. 2004). Their field 8, located at  $R \sim 12$  kpc), contains only four stars believed to be stream members, all moving with large negative velocities,  $-480 \lesssim v_{\text{hel}} \lesssim -560$  km s $^{-1}$ . The distance of the stream in this field is found to be virtually identical to the distance of M31 (McConnachie et al. 2003).

In the stream field, our velocity histogram contains 54 stars with  $v_{\text{hel}} \leq -460$  km s $^{-1}$  in the primary

cold population, 40 of which have  $v_{\text{hel}} \leq -500 \text{ km s}^{-1}$ . All previous studies of M31’s giant southern stream combined have only found five stars with  $v_{\text{hel}} \leq -500 \text{ km s}^{-1}$  (1 star in mask #1 of Guhathakurta et al. 2005a and 1 and 3 stars in fields 6 and 8 of Ibata et al. 2004, respectively). Given these statistics, we are investigating a largely unexplored region of radial velocity space for the giant southern stream.

In fitting the giant southern stream to models, Fardal et al. (2005) do not use the inner Ibata et al. (2004) pointing noting that the data may be largely contaminated by M31 disk stars. Therefore, the present study represents an important check on their models for the orbit of the stream at small radii from the nucleus of M31. For a distance along the stream of 1.6 degrees (the location of our H13s field), their simplest model (radial period of 1.7 Gyrs, apocenter 119 kpc, and pericenter 2.2 kpc) predicts that the velocity of the stream should be  $\sim -510 \text{ km s}^{-1}$ . Thus, their prediction is in excellent agreement with our measured value of  $\bar{v}_1 = -513 \text{ km s}^{-1}$ . Other orbits, and further details for this orbit, are given in Fardal et al. (2005)

## 7.2. Nature of the Secondary Cold Component

As mentioned earlier, the H13s velocity histogram shown in Figure 9 shows two prominent kinematically cold populations of stars. We now consider the second population at  $\bar{v}_2 = -417 \text{ km s}^{-1}$ , both from the standpoint of it being a new stream or a part of/associated with the giant southern stream or, alternatively, being related to M31’s outer disk.

### 7.2.1. Satellite Debris Trail?

Studies of the Milky Way have shown that multiple streams can exist along a single line of sight (e.g., Newberg et al. 2002). Numerical simulations (e.g., Bullock, Kravtsov, & Weinberg 2001) also predict large numbers of halo streamers, some of which may overlap. Disentangling this substructure represents an important step in quantifying the number density of streams and therefore testing CDM and hierarchical clustering scenarios for structure formation. The secondary velocity peak in our H13s field identified above may represent a new halo tidal stream, superimposed on the giant southern stream. Such a stream has not been detected in star-count maps of M31. However, this is not surprising given the close location of our field to the disk of M31 which produces large overdensities in the star-count map that could mask any underlying substructure from a stream. The locations of the 29 stars in the secondary peak are distributed smoothly over the entire DEIMOS masks, suggesting that the spatial scale of this population is larger than the size of a mask ( $\sim 16'$ ).

An alternative suggestion is that the secondary peak represents a wrapped around component of the giant southern stream itself. If confirmed as a stream component, the secondary velocity peak in our data could set very important constraints on the orbit of the stream and the nature of the progenitor. As we discussed in § 2, several groups have constructed dynamical models to better understand the nature of the Andromeda stream and its progenitor. These models make testable predictions for where debris from the progenitor may lie. Although, the wide range of models presented by these groups (see Font et al. 2005; Fardal et al. 2005 for details) do contain models that show a progenitor orbit that passes near the location of H13s twice (see Fig. 8 of Fardal et al. 2005), during each such passage the stars are predicted to be moving in very different phases. This results in large velocity offsets during each passage and therefore are inconsistent with the present observations. Similarly, the best two orbital fits of Ibata et al. (2004) should not produce the secondary peak at its observed location. In that model, the stream reaches its maximum velocity on the

north-west side of M31 and then falls back to a location south of M31’s disk. The predicted velocity of the stream during its fall back is estimated to be  $\sim -300 \text{ km s}^{-1}$  near the projected location of H13s on the north-south plane as defined by Ibata et al. However, such an orbit (see Figure 4(d) of Ibata et al. 2004) predicts that the secondary population would lie almost 2 degrees east of the giant southern stream and therefore can not explain these data.

We note that the stream’s very small pericenter distance makes the post-pericentric portion of the orbit strongly dependent on the (uncertain) details of M31’s inner potential (Geehan et al. 2005). The test particle orbit approximation used in the simulations above is clearly an oversimplification. More realistic modelling using  $N$ -body satellites (e.g., Fardal et al. 2005) shows that although the secondary peak in these data can not be reproduced by the stream’s orbit, reasonable orbits can be derived that connect several other prominent features/satellites of M31 with the stream: Northern Spur, M32, And NE, and a concentration in the planetary nebulae system discovered by Merrett et al. (2003). Connecting these features with the stream is possible given that the phase of the progenitor is unknown (i.e., M32 has an inconsistent radial velocity with stream stars in its present location, however, its present location could be one radial orbit ahead of the visible debris). Better orbital calculations to narrow down the progenitor and orbit of the stream require more observational constraints, especially in the locations close to M31 where the stream’s orbit is not well constrained.

We can also address the nature of the secondary peak in our velocity histogram, and whether or not it may be related to the stream, by investigating the chemical composition of stars in the peak. In Figure 10, we present a three-panel view of the velocity histogram (top), photometric  $[\text{Fe}/\text{H}]$  estimate vs. radial velocity (middle), and spectroscopic  $[\text{Fe}/\text{H}]$  estimate vs. radial velocity (bottom) for the stream field H13s. The middle and bottom panel of this diagram indicate that the mean metallicity, and metallicity dispersion, of the populations in the primary and secondary peaks are very similar. The only difference in the photometric metallicity distribution of stars in the two peaks is a small tail with higher metallicities in the secondary population that is lacking in the primary. This difference is subtle, constrained by only a few stars in the photometric metallicity diagram and is not seen in the spectroscopic metallicity distribution.

In Figure 8, we fit the metallicity distributions of these two kinematically distinct populations to Gaussians and find that indeed the distributions are very similar. Specifically, for the primary component in our velocity histogram we find  $\langle [\text{Fe}/\text{H}] \rangle = -0.47$  ( $\sigma([\text{Fe}/\text{H}]) = 0.20$ ) and for the secondary peak we find  $\langle [\text{Fe}/\text{H}] \rangle = -0.42$  ( $\sigma([\text{Fe}/\text{H}]) = 0.23$ ). Although the similar nature of the metallicity distributions in these two peaks naively suggests a similar origin for the stars, we note that the mean metallicity and metallicity dispersion of stars in the disk of M31 are also similar to those of the stream (Reitzel et al. 2005, in preparation). Therefore, from these data alone, it is equally likely that the secondary peak represents some component of the disk of M31 (e.g., a warp or an overdensity induced by satellite interaction — see § 7.2.2).

Another possible variation could be that the observed secondary velocity peak does not necessarily represent a different part of the orbit of the giant stream, but rather some unbound debris that is orbiting differentially from the main body of the stream. Future simulations with added constraints from these data and future observations (see § 8) will explore these possibilities and likely shed light on any relation of this population to the giant southern stream.

### 7.2.2. M31 Disk Feature?

We noted earlier that the metallicity distribution of stars in the secondary peak are similar to the disk field H13d (although they are at odds with the metallicity reported for the extended disk of M31 by Ibata et al. 2005). The Ibata et al. (2005) star-count map (see their Fig. 1) shows several diffuse features surrounding M31’s disk and so it is possible that a kinematically cold population of metal-rich disk stars (or disk feature) comprise the secondary peak. In fact, the expected blueshift of stars in M31’s disk at the location of H13s agrees well with the location of the secondary peak in the velocity histogram. The fits of Sawa & Sofue (1981) to the H I contours of Cram, Roberts, & Whitehurst (1980) also suggest that the disk velocity at this location is similar to that measured in the secondary peak. If the secondary peak does represent disk stars this would be an important constraint on determining the extent to which the stellar disk of M31 dominates over the spheroid/halo (Worthey et al. 2005).

To test the hypothesis that the secondary cold component represents the smooth disk of M31, we have computed the  $V$ -band surface brightness that corresponds to the stars in the secondary peak of our data (29 stars with  $-460 \leq v_{\text{hel}} \leq -380 \text{ km s}^{-1}$ ). The surface brightness computation is based on first using the results of § 4 to isolate both confirmed M31 RGB stars and confirmed Milky Way dwarf stars. We note that the sampling rate and the degree of incompleteness between these two populations is similar in our field. The observed ratio of these stars, M31 RGB to foreground Galactic dwarfs, is then multiplied by the surface density of Milky Way stars predicted by a Galactic star-count model (Ratnatunga & Bahcall 1985). This surface density only enters our final surface brightness estimate in a relative sense as we will be comparing the stream field to other fields, such as the H13d disk measurement. Therefore, any absolute mismatch between the Galactic star count model and the data is not important - only variations in the degree of mismatch across the fields being considered. Finally, we normalized the measurements to the  $V$ -band surface brightness estimates obtained by Ostheimer (2002) using a *DDO51*-selected photometric sample of M31 RGB candidates. Further details of this surface brightness calculation procedure are described in Guhathakurta et al. (2005b).

We correct the projected radius along the giant southern stream to a radius in the plane of the disk,  $R_{\text{disk}}$ . For the latter, we have assumed a disk isophotal flattening of  $(b/a) = 1 - \epsilon = 0.22$  corresponding to an inclination of  $77^\circ$  (Walterbos & Kennicutt 1988) and calculated  $R_{\text{disk}} \equiv \sqrt{a^2 + [b/(1 - \epsilon)]^2}$ , where  $a$  and  $b$  are the projected distances (in kpc) of the field from the center of M31 measured along the major and minor axes, respectively.

In Figure 11, we plot this surface brightness vs.  $R_{\text{disk}}$  for five fields: (1) our H13s secondary population, (2) disk stars in the north-east major axis H13d field (see Fig. 9 and Reitzel et al. 2005, in preparation) and south-west major axis field near G1 (Reitzel, Guhathakurta, & Rich 2004), and (3) rough, but conservative, upper limits to the disk population in the south-east minor-axis fields H11 (see Fig. 9) and RG02 (Reitzel & Guhathakurta 2002). We also show an exponential disk surface brightness profiles of the form  $\mu_S \propto \exp(-R_{\text{disk}}/R_{\text{exp}})$  with  $R_{\text{exp}} = 5.9 \text{ kpc}$ . This scale length is the distance corrected (783 kpc)  $R$ -band value in Walterbos & Kennicutt’s (1988) study of M31’s disk. These results clearly show that the surface brightness of the secondary component of H13s (filled circle) is at least  $25\times$  higher than expected from the extrapolation of M31’s smooth exponential disk. This effectively rules out the smooth disk of M31 as the source of the secondary cold population in the H13s field. We note that Ibata et al. (2005) find that the extended stellar disk is a continuation of the inner disk out to 40 kpc. The radius in the disk of M31 for our H13s field is almost twice as large as this,  $\sim 75 \text{ kpc}$ .

We can further test whether the H13s secondary component represents M31 disk stars by considering

previous studies of the stream and searching for evidence of a secondary component in the velocity histograms. Although these studies have not been able to find large numbers of stars belonging to the inner parts of the stream ( $R \lesssim 25$  kpc), there have been a few studies in regions just outside this radius. The secondary peak in these data may have been undetected given low number statistics, or the fact that the radial velocity of the stream becomes more positive as the distance from M31 increases and therefore the kinematics of the stream stars may overlap with the disk stars. In contrast, if the secondary peak in our data is M31’s outer disk, then we would expect its velocity to be roughly constant at all radii along the stream ( $\bar{v}_2 = -417$  km s $^{-1}$ ). We have shown approximate locations of three other studies of the giant southern stream in Figure 1, the a3 field (Guhathakurta et al. 2005a), and the F6 and F8 fields (Ibata et al. 2004).

At  $R \sim 33$  kpc, Guhathakurta et al. (2005a) found 45 M31 stream RGB stars centered at a velocity of  $-458$  km s $^{-1}$  (field a3). As expected, given the further location of their field from M31, stream stars do not have a large contrast with the potential secondary peak. We present their velocity histogram in the bottom panel of Figure 12. Interestingly, there is a very small peak at  $v_{\text{hel}} \sim -420$  km s $^{-1}$  in their data however it is also consistent with the tail of the primary stream population. Better constraints can be derived from the  $R \sim 25$  kpc (field 6) Ibata et al. (2004) study<sup>5</sup>. Although they attribute 30 stars to the stream (see their Fig. 1, right panel), only 22 of these have  $v_{\text{hel}} \lesssim -450$  km s $^{-1}$ . The remaining 8 stars have  $-440 \lesssim v_{\text{hel}} \lesssim -390$  km s $^{-1}$ , consistent with the mean radial velocity of our H13s secondary peak. These data are presented in the third panel of Figure 12. Besides our study (second panel of Fig. 12), the only other spectroscopic observations of the inner stream are the innermost field (field 8) of Ibata et al. (2004) at  $R \sim 12$  kpc where they find 2–4 stream stars with  $v_{\text{hel}} \sim -500$  km s $^{-1}$  and a group of 7 stars at  $v_{\text{hel}} \sim -400$  km s $^{-1}$ . These data are shown in the top panel of Figure 12.

The histograms in Figure 12 show mild evidence of a trend similar to what we would expect if the secondary peak consists of M31 disk stars. The ratio of the number of stars in the secondary velocity peak (between the dashed lines) to the primary peak appears to decrease as a function of increasing radius. We have defined the secondary peak here based on the Ibata et al. (2004) F8 field, which shows the largest contrast between secondary and primary populations. To a first approximation, we can quantify this trend by simply counting the number of stars in each component directly from Figure 12. Over the projected radial distance of the stream in the four pointings shown in Figure 12 (12–33 kpc), the star-count map of M31 (Figure 1) does not show any obvious changes in the surface density of the giant southern stream. If we assume that the surface density of the giant southern stream (primary peak) is constant, then the ratio of secondary peak to primary peak stars effectively gives us the radial surface brightness profile of the secondary component. Since the apparent brightness and metallicity ranges of stars in both peaks is virtually identical, taking the ratio also eliminates any possible biases (e.g., there may be variations in the degree of completeness from one study to another, but this should affect both primary and secondary peak populations equally). If the outer disk is responsible for the secondary peak, then the radial dependence of this surface brightness should follow the measured exponential profile of M31’s disk. We compute  $R_{\text{disk}}$  for each of the fields in Figure 12 as discussed earlier for H13s. A radial density distribution based on these numbers is shown in Figure 13. Also shown is an exponential disk with  $\mu_S \propto \exp(-R_{\text{disk}}/5.9 \text{ kpc})$  (solid). This exponential disk profile for this scale length is in gross disagreement with the radial secondary peak data, confirming that this population does not look like the smooth disk of M31. For comparison, the dashed line illustrates that in order to fit these data with such a model, the scale length of the disk would have to be very large:  $R_{\text{exp}} \approx 40$  kpc. Adopting a less extreme inclination for the disk — say a flattening of

---

<sup>5</sup>Ibata et al. (2004) do not provide velocity histograms for their data so we have constructed them from their Figure 1.

$(b/a) \equiv 1 - \epsilon = 0.31$  (Worthey et al. 2005) — does not resolve the mismatch. Since there is no convincing evidence for a secondary population in the bottom two panels of Figure 12, we have plotted these data points as upper limits in Figure 13. The size of the arrow indicates the random error associated with these points. We note however that if the surface density of the giant southern stream (primary peak) decreases with increasing distance from the plane of M31, then our outer data points have been artificially “boosted” and a model with a somewhat smaller scale length will fit the secondary peak data. We also note that a very small number of smooth spheroid stars may exist in each of the primary and secondary velocity peaks and have not been removed. This contribution is known to be very small and does not affect the results.

Taken together, both the surface brightness and radial density distribution of the secondary peak in H13s argue against it consisting of M31 smooth disk stars. It is however possible that this cold population represents some kind of disk feature, possibly tidally ripped from M31’s smooth disk during a satellite accretion event. Such a warp is known to exist along the major axis of M31 (e.g., the Northern Spur) but has not been reported on the minor axis.

## 8. Future Studies

Despite the many studies that have looked at Andromeda’s giant southern stream, several important issues remain unresolved including the exact orbit of the stream and the nature of the progenitor system that created it. The secondary peak detected in this study adds to the observational database and will surely invite different groups to construct new models to explain this feature. Future Keck/DEIMOS observations should target spectroscopy fields in the inner regions of the giant southern stream to improve the statistics currently constrained solely by the Ibata et al. (2004) detection (a few stars in the stream at  $R \sim 12$  kpc). The multi-object spectroscopic method employed in this study will be very efficient in the inner regions of the stream and should detect  $\sim 100$  bonafide stream stars per DEIMOS mask. It would also be interesting to conduct observations in a field directly to the north-east of our current pointing, stepping by  $\approx 1$  degree parallel to the major axis. Observing a field at the same radial distance, but off the stream, should confirm the presence of the secondary peak found in this study if it is related to the disk of M31.

Recent ultra-deep *HST* observations have now been taken in overlapping fields to this study (T. Brown 2005, private communication). These observations, in H13s, H11, and H13d will complement our study by providing additional constraints. The mean ages of stars in these fields, and the spread in ages, will be directly measured from fitting the morphology of the main-sequence turnoff in those data with isochrones and by comparing the numbers of stars in various evolutionary phases with numerical simulations. A relative comparison of the CMDs of the H13s and H13d fields could potentially help resolve the stream from the outer disk in these inner regions.

Wide-field CFHT/MegaCam images (1 degree<sup>2</sup>) have also been obtained directly covering our H13s and H11 fields. These images will provide much deeper star counts than in the Ibata et al. (2005) map and will allow us to search for lower surface brightness features in these fields. The MegaCam images will directly provide detailed starcounts as a function of radius over the inner regions of the giant stream. These will be very important in the face of our discovery of a secondary population in our H13s field. The new star-count map will also better define the width and northern sharp edge of the giant stream, both of which are important inputs into constraining models for the stream’s orbit. These observations are currently being reduced and will be published in a forthcoming paper.

## 9. Conclusion

We present Keck/DEIMOS observations of red giant stars in three fields in the Andromeda spiral galaxy: a field on the giant southern stream, a minor-axis spheroid field, and a major-axis disk field. In this paper, we discuss the kinematics and chemical composition of stars in the stream field at a projected distance of  $R \sim 21$  kpc from M31’s center. The disk and spheroid fields will be addressed in future papers.

We isolate RGB stars in M31 by removing foreground Galactic dwarf star contaminants through probability distribution functions calculated from a training set of known RGB and dwarf stars. These functions combine four individual parameters — (1) radial velocity, (2) NaI equivalent width (surface gravity sensitive), (3) position in the CMD, and (4) comparison between photometric and spectroscopic  $[\text{Fe}/\text{H}]$  estimates — to compute a likelihood that any given object is an M31 RGB star or a Milky Way dwarf star. The M31 RGB sample shows the cleanest detection to date of the inner part of the giant southern stream: a kinematically-cold population ( $\sigma(v_1) = 16 \text{ km s}^{-1}$ ) of 50 stars moving with a mean heliocentric velocity of  $\bar{v}_1 = -513 \text{ km s}^{-1}$ . These stars are found to be metal-rich, with a mean metallicity  $\langle [\text{Fe}/\text{H}] \rangle = -0.47$ , and a small metallicity dispersion. We also find clear evidence for a second population of stars that is also moving with a relatively large negative radial velocity with respect to M31’s systemic velocity:  $\bar{v}_2 = -417 \text{ km s}^{-1}$  that is comparably cold:  $\sigma(v_2) = 16 \text{ km s}^{-1}$ ). This second cold population has never been reported before. A close look at previous spectroscopic observations reveals evidence that this second group of stars is not associated with the smooth disk of M31, but rather may represent a new satellite debris trail, a wrapped around component of the giant southern stream, or a tidally-disrupted population of disk stars. Future observations of the inner regions of the stream will help constrain models for its orbit and put better limits on which, if any, of M31’s satellites may be the progenitor.

We wish to thank Peter Stetson and Jim Hesser for help in acquiring the CFHT/MegaCam imaging fields for this project. We are also grateful to Peter Stetson and James Clem for providing programs and for many useful discussions regarding the astrometry of the CFHT images. We wish to thank Carynn Luine for help with the verification of the radial velocity measurements and Leo Girardi for providing us with an extensive grid of theoretical stellar isochrones. We also acknowledge Tom Brown for making available unpublished results based on Cycle 13 *HST* observations. J.S.K. is supported by NASA through Hubble Fellowship grant HF-01185.01-A, awarded by the Space Telescope Science Institute, which is operated by the Association of Universities for Research in Astronomy, Incorporated, under NASA contract NAS5-26555. This project was also supported by NSF grant AST-0307966 and NASA/STScI grant GO-10265.02 (J.S.K., P.G., and K.M.G.), an NSF Graduate Fellowship (K.M.G.), NSF grant AST-0307931 (R.M.R. and D.B.R.), and NSF grants AST-0307842 and AST-0307851, NASA/JPL contract 1228235, the David and Lucile Packard Foundation, and The F. H. Levinson Fund of the Peninsula Community Foundation (S.R.M.).

## REFERENCES

- Bertin, E., & Arnouts, S. 1996, *A&AS*, 117, 393
- Bode, P., Ostriker, J. P., & Turok, N. 2001, *ApJ*, 556, 93
- Brown, T. M., Ferguson, H. C., Smith, E., Kimble, R. A., Sweigart, A. V., Renzini, A., Rich, R. M., & VandenBerg, D. 2003, *ApJ*, 592, L17
- Bullock, J., Kravtsov, A., & Weinberg, D. 2001, *ApJ*, 548, 33



- Carretta, E. & Gratton, R. G. 1997, *A&AS*, 121, 95
- Cram, T. R., Roberts, M. S., & Whitehurst, R. N. 1980, *A&AS*, 40, 215
- Fardal, M. A., Babul, A., Geehan, J. J., & Guhathakurta, P. 2005, *MNRAS*, submitted (astro-ph/0501241)
- Ferguson, A. M. N., Johnson, R. A., Faria, D. C., Irwin, M. J., Ibata, R. A., Johnston, K. V., Lewis, G. F., & Tanvir, N. R. 2005, *ApJ*, 622, L109
- Ferguson, A. M. N., Irwin, M. J., Ibata, R. A., Lewis, G. F., & Tanvir, N. R. 2002, *AJ*, 124, 1452
- Font, A. S., Johnston, K. V., Guhathakurta, P., Majewski, S. R., & Rich, R. M. 2005, *AJ*, submitted (astro-ph/0406146)
- Geehan, J. J., Fardal, M. A., Babul, A., & Guhathakurta, P. 2005, *MNRAS*, submitted (astro-ph/0501240)
- Girardi, L., Bertelli, G., Bressan, A., Chiosi, C., Groenewegen, M. A. T., Marigo, P., Salasnich, B., & Weiss, A. 2002, *A&A*, 391, 195
- Guhathakurta, P., et al. 2005a, *AJ*, submitted (astro-ph/0406145)
- Guhathakurta, P., Ostheimer, J. C., Gilbert, K. M., Rich, R. M., Majewski, S. R., Kalirai, J. S., Reitzel, D. B., Cooper, M. C., & Patterson, R. J. 2005b, *Nature*, submitted (astro-ph/0502366)
- Hayashi, E., Navarro, J. F., Taylor, J. E., Stadel, J., & Quinn, T. 2003, *ApJ*, 584, 541
- Holland, S. 1998, *PASP*, 98, 609
- Ibata, R., Chapman, S., Ferguson, A. M. N., Lewis, G., Irwin, M., & Tanvir, N. 2005, *ApJ*, submitted (astro-ph/0504164)
- Ibata, R., Chapman, S., Ferguson, A. M. N., Irwin, M., Lewis, G., & McConnachie, A. 2004, *MNRAS*, 351, 117
- Ibata, R., Irwin, M., Lewis, G., Ferguson, A. M. N., & Tanvir, N. 2001, *Nature*, 412, 49
- Ibata, R., Gilmore, G., & Irwin, M. J. 1994, *Nature*, 370, 194
- Johnston, K. V. 1998, *ApJ*, 495, 297
- Kalirai, J. S., et al. 2001, *AJ*, 122, 257
- Klypin, A., Kravtsov, A. V., Valenzuela, O., & Prada, F. 1999, *ApJ*, 522, 82
- Majewski, S. R., Skrutskie, M. F., Weinberg, M. D., & Ostheimer, J. C. 2003, *ApJ*, 599, 1082
- Mathewson, D. S., Cleary, M. N., & Murray, J. D. 1974, *ApJ*, 190, 291
- McConnachie, A. W., Irwin, M. J., Ibata, R. A., Ferguson, A. M. N., Lewis, G. F., & Tanvir, N. 2003, *MNRAS*, 343, 1335
- Merrett, H. R., et al. 2003, *MNRAS*, 346, L62
- Monet, D. G., et al. 1998, *USNO-A2.0* (Flagstaff: US Naval Obs.), CD-ROM
- Moore, B., Ghigna, S., Governato, F., Lake, G., Quinn, T., Stadel, J., & Tozzi, P. 1999, *ApJ*, 524, L19

- Morrison, H. L., Harding, P., Hurley-Keller, D., & Jacoby, G. 2003, *ApJ*, 596, L183
- Newberg, H. J. et al. 2002, *ApJ*, 569, 245
- Ostheimer, J. C. 2002, Ph.D. dissertation, University of Virginia
- Ratnatunga, K. U., & Bahcall, J. N. 1985, *ApJS*, 59, 63
- Reitzel, D. B., & Guhathakurta, P. 2002, *AJ*, 124, 234
- Reitzel, D. B., Guhathakurta, P., & Rich, R. M. 2004, *AJ*, 127, 2133
- Rutledge, G. A., Hesser, J. E., & Stetson, P. B. 1997, *PASP*, 109, 907
- Rutledge, G. A., Hesser, J. E., Stetson, P. B., Mateo, M., Simard, L., Bolte, M., Friel, E. D., & Copin, Y. *PASP*, 109, 883
- Schlegel, D. J., Finkbeiner, D. P., & Davis, M. 1998, *ApJ*, 500, 525
- Sawa, T., & Sofue, Y. 1981, *Astron. Soc. of Japan Publications*, 33, 665
- Searle, L., & Zinn, R. 1978, *ApJ*, 225, 357
- Spergel, D. N., et al. 2003, *ApJS*, 148, 175
- Stetson, P. B., McClure, R. D., & VandenBerg, D. A. 2004, *PASP*, 116, 1012
- Stetson, P. B. 1979, *AJ*, 84, 1056
- Walterbos, R. A. M., & Kennicutt, R. C., Jr. 1988, *A&A*, 198, 61
- Worthey, G., Espana, A., MacArthur, L., & Courteau, S. 2005, *ApJ*, submitted (astro-ph/0410454)
- Yanny, B., et al. 2003, *ApJ*, 588, 824

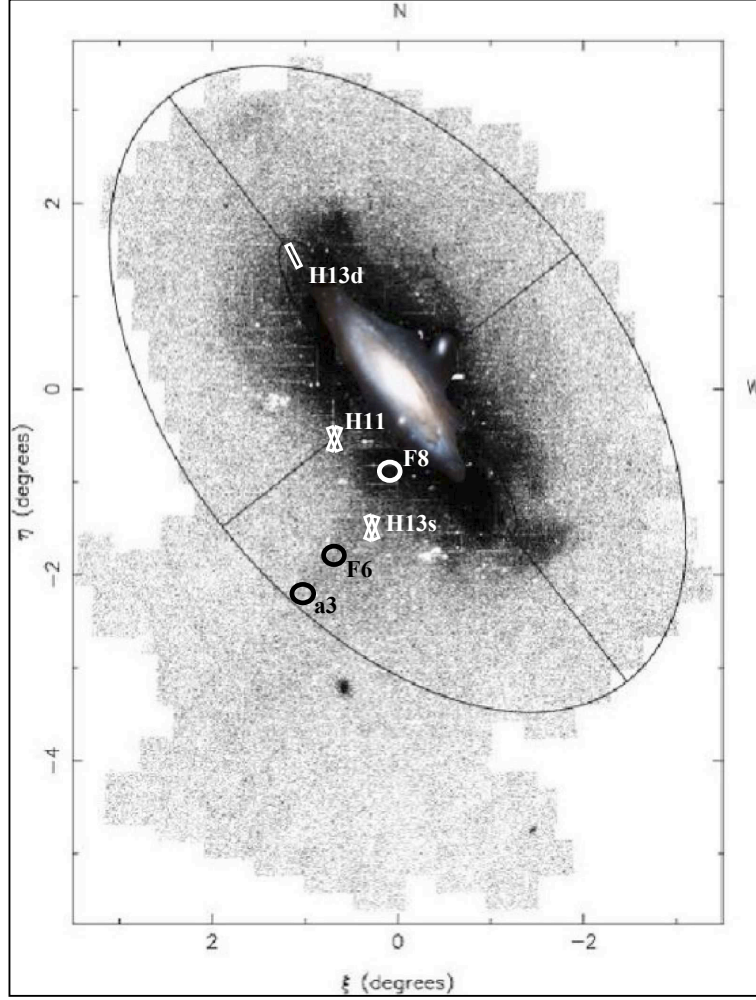


Fig. 1.— The location of our three spectroscopic fields H13s, H11, and H13d, are shown as rectangles superimposed on a star-count map of M31 (Ibata et al. 2005). Approximate locations of other studies of the giant southern stream are also shown as circles (to be discussed later). A scaled DSS image of M31 is shown at the centre of the star-count map.

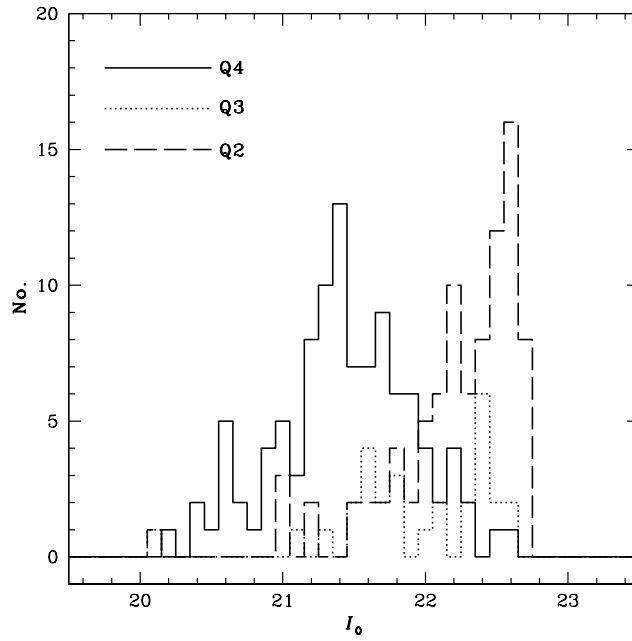


Fig. 2.— Distribution of  $I_0$  magnitude for spectroscopic targets in the H13s stream field grouped according to their spectral quality codes:  $Q = 2, 3$ , and  $4$ . The distributions confirm that the faintest objects in our spectroscopic sample ( $I_0 \gtrsim 22$ ) are generally the ones for which the radial velocity measurement fails presumably as a result of their poor spectral quality (i.e., relatively low S/N).

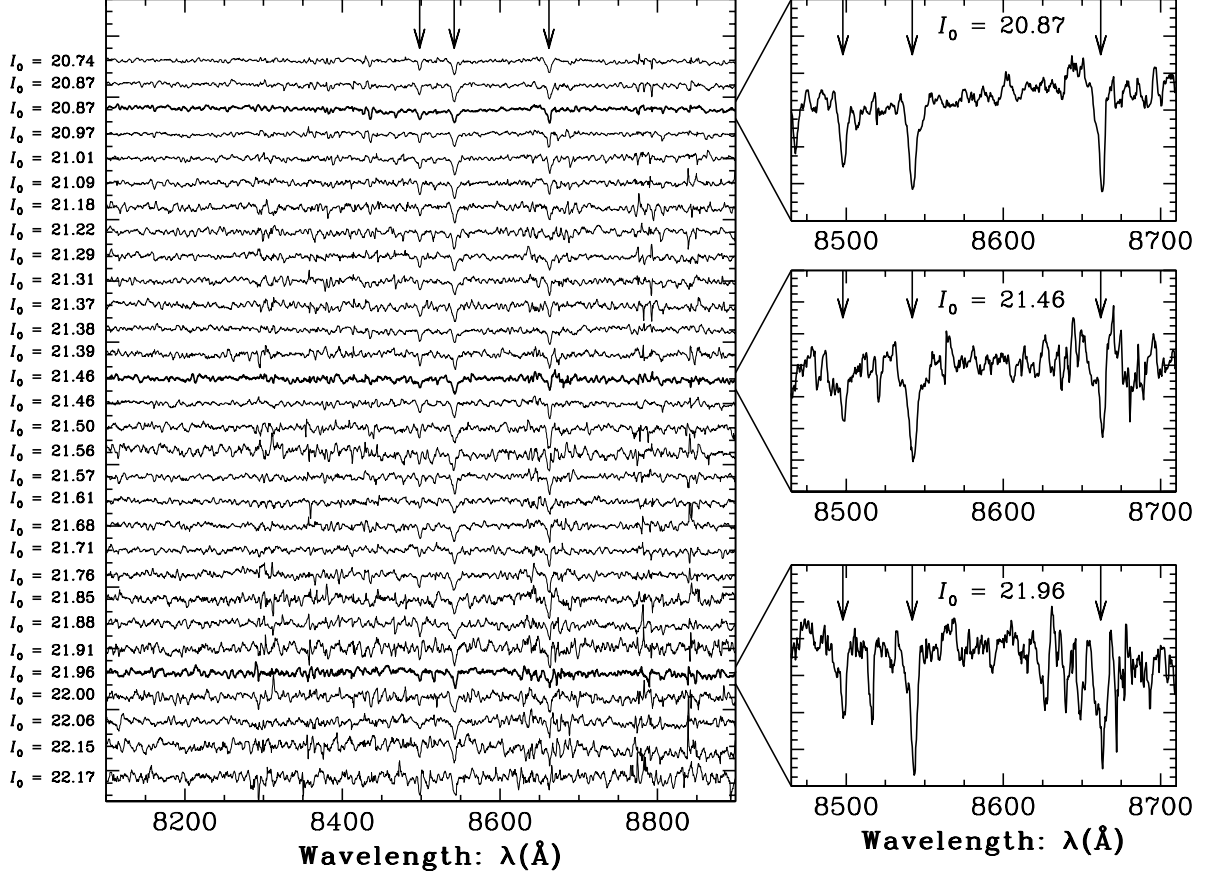


Fig. 3.— Spectra for 30 M31 stream RGB stars, with  $Q = 4$ , in the brightness range  $20.7 \lesssim I_0 \lesssim 22.2$  showing only the wavelength range 8100–8900 $\text{\AA}$ . The spectra have been corrected to zero velocity, normalized at  $\lambda \sim 8500\text{\AA}$ , offset in  $y$  arbitrarily, and smoothed using a 10 pixel (3 $\text{\AA}$ ) boxcar function for illustration purposes only. Arrows mark the locations of the Ca II triplet: 8498, 8542, and 8662 $\text{\AA}$ . The panels on the right present a closer look at the Ca II triplet region for three arbitrarily chosen stars.

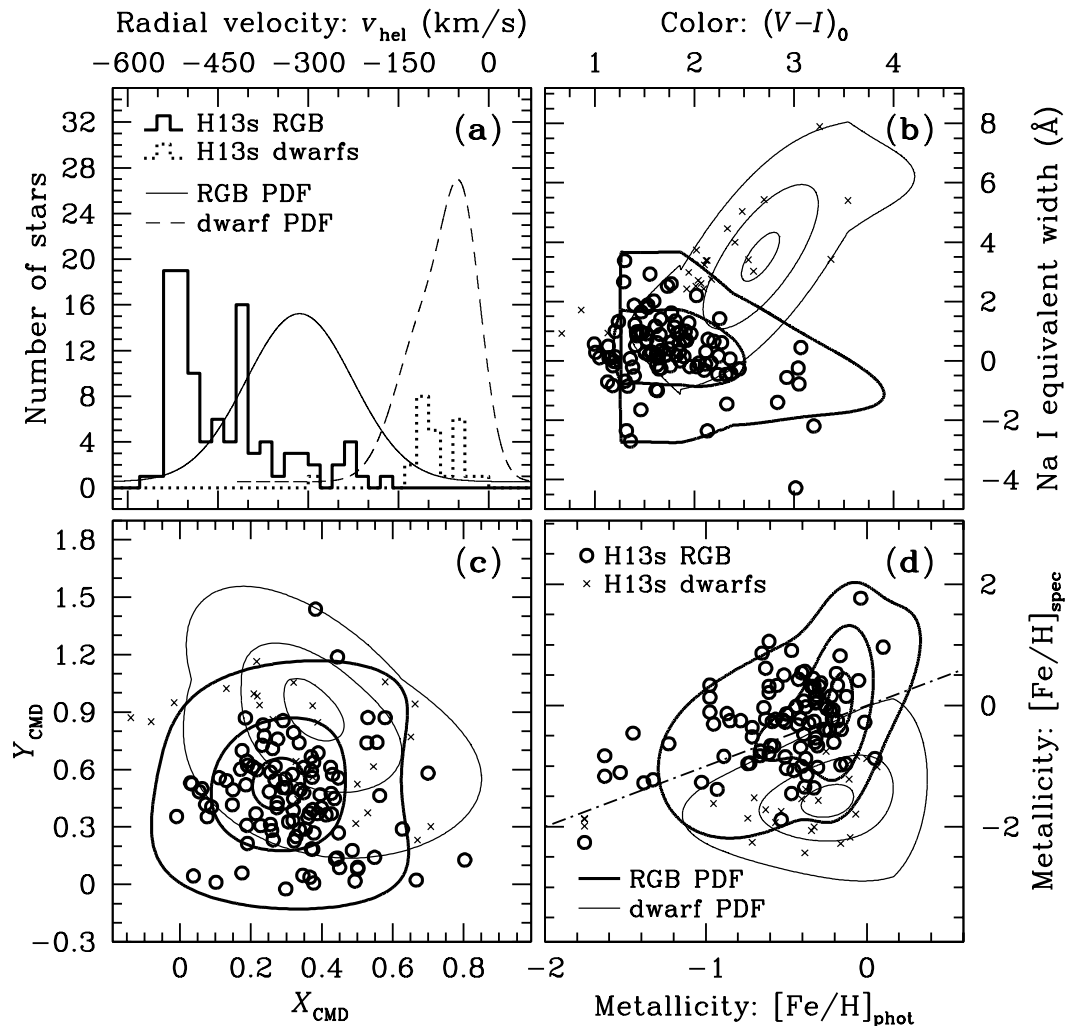


Fig. 4.— Four of the photometric/spectral diagnostics that are used to distinguish M31 RGB stars from foreground Milky Way dwarf contaminants are shown. The probability distribution functions for the training sets are given as darker solid curves for RGB stars and dashed (or thinner curves) for the dwarfs, in each of the 4 panels: (a) radial velocity, (b) Na I equivalent width, (c) position in the CMD, and (d) comparison between photometric and spectroscopic  $[\text{Fe}/\text{H}]$  measurements. Also shown are the positions of H13s stars within each diagnostic. The computed RGB stars are shown as a solid histogram in (a) and as large open circles in (b), (c), and (d). Similarly, the computed dwarf stars in H13s are shown as a dashed histogram in (a) and as small crosses in (b), (c), and (d). In all panels, the confirmed RGB and dwarf stars appear to follow the appropriate probability distribution functions. Note that the RGB velocity histogram in (a) is offset from the training set distribution due to the large negative velocity of stream stars relative to M31’s systemic velocity.

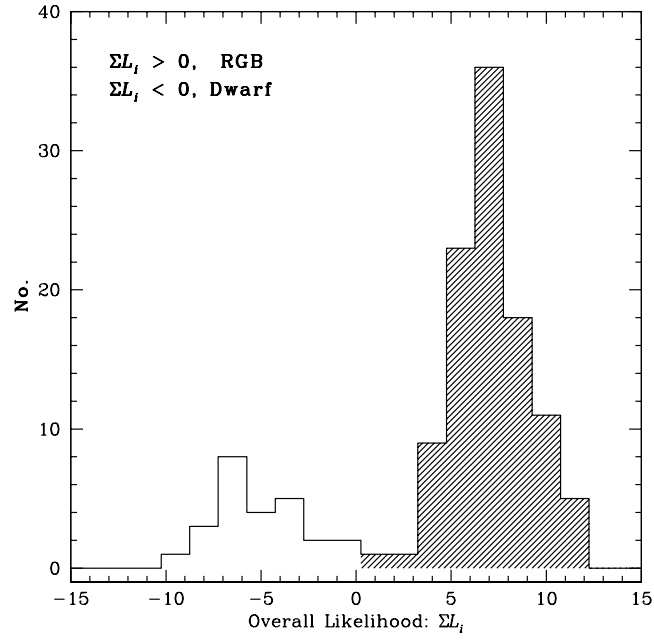


Fig. 5.— The individual probabilities of a star being an RGB or a dwarf from the four diagnostics in Figure 4 are combined to yield an overall likelihood,  $\Sigma L_i$ . The results show a very nice bi-modal distribution with a minimum near 0. The shaded histogram ( $\Sigma L_i > 0$ ) represents the RGB stars, whereas the open histogram ( $\Sigma L_i < 0$ ) shows the dwarfs.

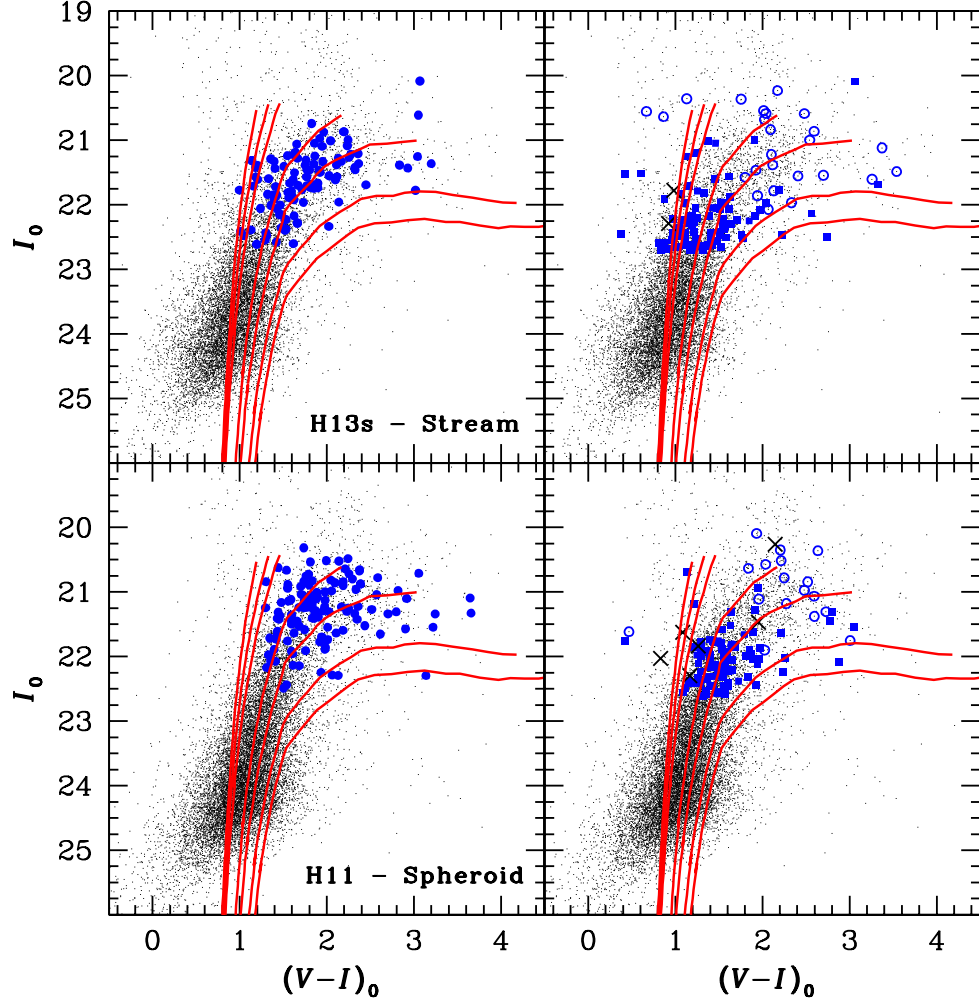


Fig. 6.— Color-magnitude diagrams for the H13s (top) and H11 (bottom) fields. Bonafide M31 RGB stars (i.e., those that have spectral quality  $Q = 3$  or 4 and have passed the foreground dwarf star contaminant screening in § 4) are shown in the left-hand panels as large filled circles. The right-hand panels show Milky Way dwarf stars (open circles),  $Q = 2$  objects for which there is no reliable radial velocity measurement (filled squares), and background field galaxies (crosses). The smaller dots represent stars in a larger imaging region surrounding the spectroscopic fields. A detailed discussion of these data and isochrones is given in § 5.1.



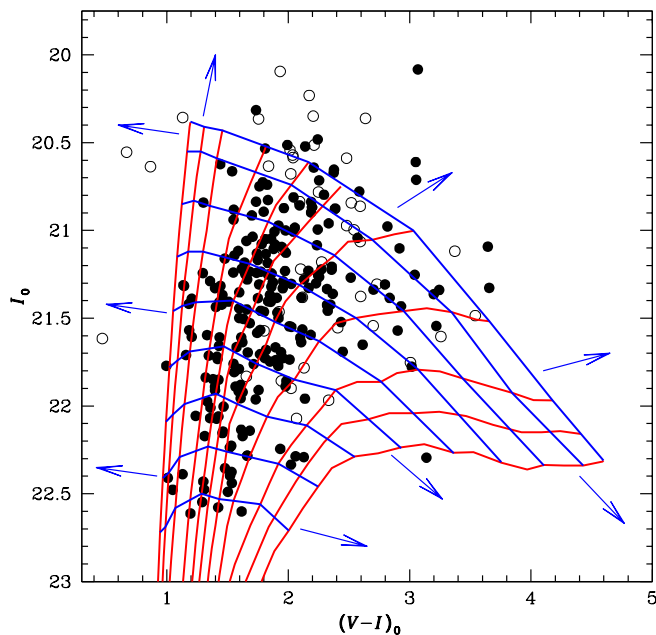


Fig. 7.— A sample grid that was used to measure photometric metallicities is shown. Eleven representative isochrones with ages of 12.6 Gyr and  $0.0001 < Z < 0.03$  or  $-2.3 < [\text{Fe}/\text{H}] < +0.2$  (Girardi et al. 2002) are overlaid on all confirmed RGB stars in the H13s and H11 fields (filled circles). Milky Way dwarf stars are shown as open circles. “Cross-isochrones” are also shown as discussed in § 5.2. Photometric metallicities of all stars were measured by using a nearest neighbor approach within a much more finely spaced grid of 300 isochrones. Arrows indicate the extrapolation directions.

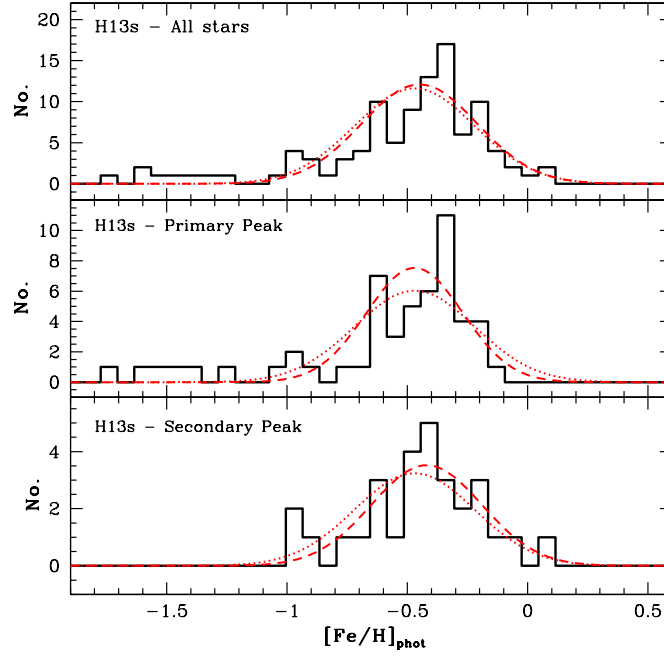


Fig. 8.— The photometric metallicity distributions for H13s is shown. The top panel presents the data for all M31 RGB stars in the field, whereas the middle and bottom panels present only the data in the primary and secondary velocity peaks (to be discussed in § 6.2). The dashed curves show Gaussian fits to each population. For the entire sample (top), we find  $\langle [\text{Fe}/\text{H}] \rangle = -0.45$ ,  $\sigma([\text{Fe}/\text{H}]) = 0.24$ . The dotted curves shows the metallicity distribution of stars in our spheroid field, H11, which is clearly found to be similar to our stream field.

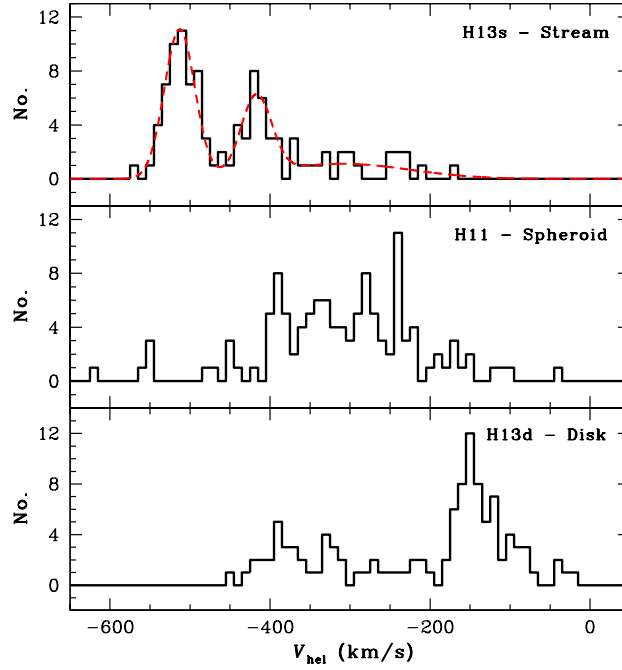


Fig. 9.— The velocity histograms for our three fields show a very clean separation of the stream, spheroid and disk of M31. The stream component contains a dynamically cold population of highly blueshifted stars,  $\bar{v}_1 = -513 \text{ km s}^{-1}$ , the spheroid contains a hotter population of stars moving at M31’s systemic velocity  $v_{\text{hel}} \sim -300 \text{ km s}^{-1}$ , and the disk in the north-east quadrant shows a cold population of low velocity stars (as expected given the disk’s rotation in this quadrant). Also shown is a triple Gaussian fit to the two prominent stream peaks, as well as the underlying smooth spheroid, in the top panel (see §6.2).

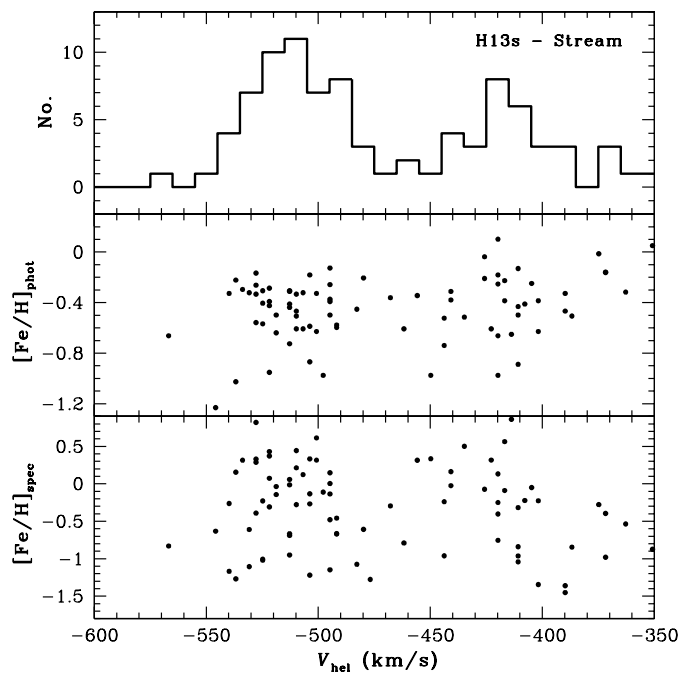


Fig. 10.— The velocity histogram, photometric metallicity vs. velocity, and spectroscopic metallicity vs. velocity distributions for the bimodal velocity peaks in the stream field. The metallicities of the two populations in the dynamically cold peaks are clearly similar (see § 7.2 for a discussion). The larger spread in the spectroscopic metallicity distribution is caused by the propagation of the relatively large random errors in the Ca II triplet equivalent width measurements. Only stars with  $v_{\text{hel}} \leq -350 \text{ km s}^{-1}$  are shown.

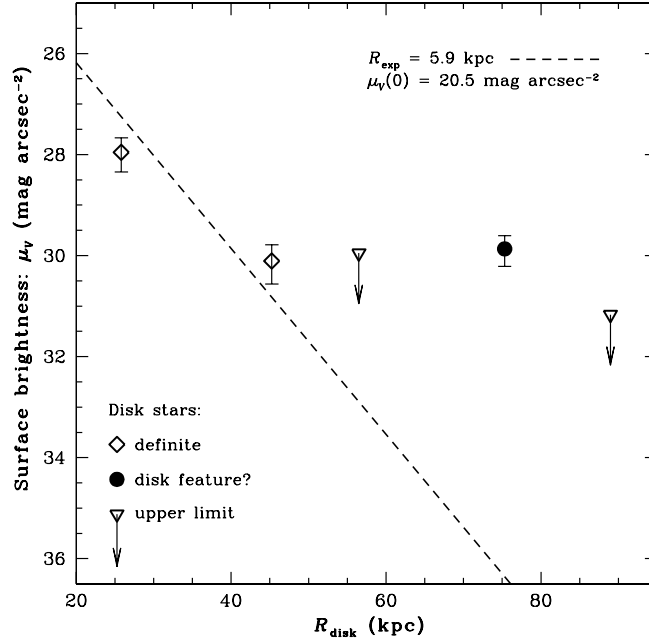


Fig. 11.— Plot of the radial surface brightness profile in the  $V$  band showing the secondary component in the H13s field as a filled circle, disk stars in the major-axis fields H13d and G1 (Reitzel et al. 2004) as open diamonds, and upper limits to the disk population in the minor-axis fields H11 and RG02 (Reitzel & Guhathakurta 2002) as open triangles with arrows. The error bars represent Poisson errors. The surface brightnesses have been calculated as discussed in § 7.2.2 and Guhathakurta et al. (2005b). Also plotted is an exponential profile:  $\mu_S \propto \exp(-R_{\text{disk}}/R_{\text{exp}})$ , where  $R_{\text{exp}}$  is taken to be 5.9 kpc (Walterbos & Kennicutt 1988). The H13s secondary component (filled circle) is clearly too bright to be related to M31’s smooth disk.

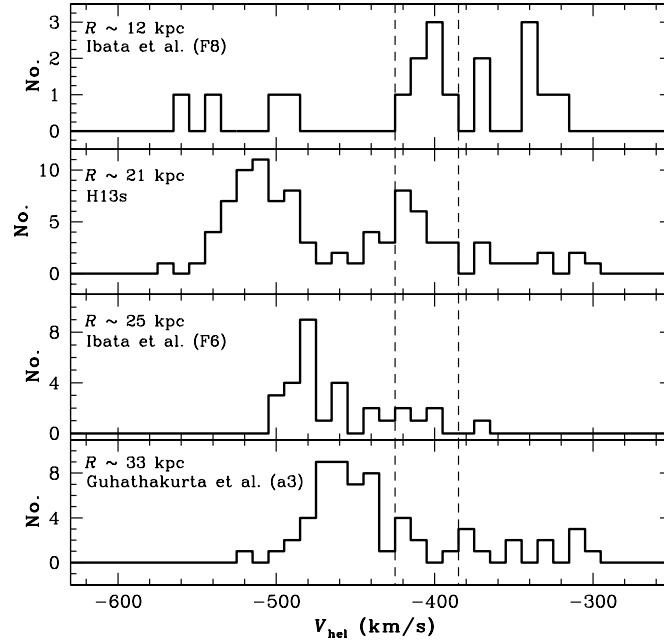


Fig. 12.— Radial velocity histograms for various studies of M31’s giant southern stream are shown in order of increasing radius. The Ibata et al. (2004) fields 8 and 6 data are shown in the top and third panel, respectively. Our H13s data are shown in the second panel, and the Guhathakurta et al. (2005a)  $R \sim 33$  kpc field a3 is shown in the bottom panel. As the radial distance from M31 increases, the ratio of the number of stars in the secondary-to-primary peak decreases (suggesting that the secondary peak may be related to M31’s outer disk — however, see § 7.2.2). The dashed lines indicate the region of velocity space within which we count secondary peak stars. Only stars with  $v_{\text{hel}} \leq -300 \text{ km s}^{-1}$  are shown in this figure.

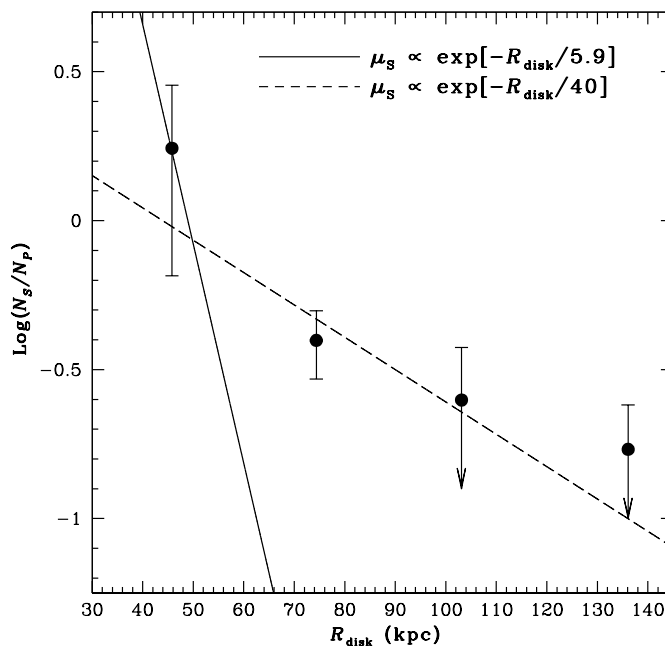


Fig. 13.— Ratio of stars in the secondary velocity peak to those in the primary velocity peak plotted as a function of radius in the plane of M31’s disk (see § 7.2.2). The data points are found to be inconsistent with a smooth disk following a  $\mu_s \propto \exp(-R/R_{\text{exp}})$  surface brightness law with  $R_{\text{exp}} = 5.9$  kpc (solid line). This profile, as well as the profile with  $R_{\text{exp}} = 40$  kpc, have both been arbitrarily scaled in the vertical direction. The outer two data points are shown as upper limits, with an arrow signifying the size of the random error bar.

Table 1. Keck/DEIMOS Observations of M31<sup>1</sup>

Field Location	Field ID	Mask ID	$\alpha$ (J2000) (h:m:s)	$\delta$ (J2000) ( $^{\circ}$ : $'$ : $''$ )	$R_{\text{proj}}$ (kpc)	Pos. Angle ( $^{\circ}$ )	Exp. Time <sup>2</sup> (s)	No. Targets <sup>2</sup>	Airmass
Giant Southern Stream	H13s	f2_1	00:44:14.76	+39:44:18.2	21	+21.0	3600	133	1.84
		f2_2	00:44:14.76	+39:44:18.2	21	-21.0	3600	137	1.33
South-East Minor Axis (Spheroid)	H11	f1_1	00:46:21.02	+40:41:31.3	12	+21.0	3600	136	1.15
		f1_2	00:46:21.02	+40:41:31.3	12	-21.0	3600	135	1.07
North-East Major Axis (Disk)	H13d	f3_1	00:49:04.80	+42:45:22.6	26	+27.8	3600	145	1.10
		f3_2	00:49:04.80	+42:45:22.6	26	+27.8	3600	144	1.32

<sup>1</sup>All observations were obtained on 2004 September 20 (UT).

<sup>2</sup>2 targets were observed twice on each of H13s and H11, and 53 targets were observed twice on H13d; see §§ 3.2 & 3.5.